Lab on a Chip

PAPER

View Article Online
View Journal | View Issue

Cite this: *Lab Chip*, 2014, **14**, 4370

Coincidence detection of heterogeneous cell populations from whole blood with coplanar electrodes in a microfluidic impedance cytometer†

U. Hassan[ab] and R. Bashir*[bc]

Particle counting finds many industrial applications especially in medical healthcare. In particular, cell counting from whole blood is used pervasively for disease diagnostics. Microfluidic impedance cytometry is fast, requires a small volume of blood, can be used at point of care and can perform absolute enumeration of different cell types in the sample. Coincidence detection is very essential for accurate counting results and becomes more significant while counting specific target cells, *e.g.* $CD4^+$ or $CD8^+$ T cell count in HIV/AIDS patient blood samples. In heterogeneous samples, *e.g.* blood, cell differentiation for all coincidence occurrences is essential in addition to the coincidence detection for accurate cell enumeration. In this paper, we have characterized the coincidence detection with cell differentiation using a microfluidic impedance biochip. The pure population of leukocytes is obtained after all erythrocytes are lysed on-chip from whole blood. Leukocytes were counted electrically as they pass over coplanar microfabricated electrodes bonded to the 15 μm × 15 μm cross section counting channel while generating a bipolar pulse for each cell passage. We have developed a mathematical model to simulate the electrical cell pulse and its coincidences. We show that coincidence detection can be characterized into three main types based on the range of time delay at which the coincidence occurs. We have also characterized cell differentiation for all the three coincidence types and show that multiple coincidences of different types can also occur. We used healthy and HIV-infected patient blood samples and used our coincidence detection technique to count $CD4^+$ and $CD8^+$ T cells and show the improvement in accuracy of cell counts compared to that without coincidence detection. We have also shown the improvement in the erythrocyte counting with coincidence detection in diluted whole blood samples.

Received 27th July 2014,
Accepted 1st September 2014

DOI: 10.1039/c4lc00879k

www.rsc.org/loc

Introduction

Particle enumeration by Coulter counting was first reported in the 1950s.[1] This powerful and pervasive technique finds many applications in industry, medicine, and healthcare, especially in disease diagnostics in humans and animals. Industrial applications of particle counting include determining liquid purification by finding the size of the contaminant particles and counting yeast cells for wine industries.[2] Somatic cell count is used to determine the quality of milk and provides an indication of mastitis.[3] Other biological applications include counting particles and finding their size distribution, *e.g.* for pollen[4] and for bacteria.[5] The Coulter counting principle can also be used to detect DNA using nanopores,[6] and antigen–antibody interaction can also be found using on-chip nanopores.[7] Particle counting is not only limited to biological applications; other examples include particle detection using Geiger counters[8,9] and atomic emission spectroscopy to determine the particle size distribution in the debris.[10] Label-free cell enumeration in microfluidic biosensors requires counting all cells electrically.[11] Individual cell counting in microfluidic impedance cytometers requires a Coulter aperture with microfabricated electrodes bonded to it.[12] Cell enumeration in microfluidic devices is shown by many studies[13–15] to count leukocytes and its differential and platelets and erythrocytes.

Occurrence of the cell counts is a mathematical Poisson process[16] and coincidence can be mathematically described by Poisson clumping and can never be truly eliminated irrespective of the sample dilution.[17] Zheng *et al.* performed coincidence detection and reported the mathematical relation

[a] *Department of Electrical and Computer Engineering, University of Illinois at Urbana-Champaign, William L. Everitt Laboratory, 1406 W. Green St., Urbana, IL 61801, USA*
[b] *Micro and Nanotechnology Lab, University of Illinois at Urbana-Champaign, 208 N. Wright St., Urbana, IL 61801, USA. E-mail: rbashir@illinois.edu*
[c] *Department of Bioengineering, University of Illinois at Urbana-Champaign, 1270 Digital Computer Laboratory, 1304 W. Springfield Ave., Urbana, IL 61801, USA*
† Electronic supplementary information (ESI) available. See DOI: 10.1039/c4lc00879k

to estimate the counting errors because of coincidence effects with beads. The estimated true count (N) was obtained by the experimental count (n), sample volume (V) and the aperture volume (ΔV) using the following equation: $n = \frac{V}{\Delta V}\left(1 - e^{-\frac{\delta V}{V}N}\right)$.[18,19] However, such estimation is only valid for homogeneous particle samples. This approach also lacks the true measurement of coincidence at each time. Coincidence detection in heterogeneous samples with varying particle sizes becomes more significant. Some earlier work has been done in coincidence detection for particle counting. For industrial particle counting device manufacturers, determining the particle coincidence is significant as they are required to report the % particle coincidence of their devices as part of obtaining different International Organization for Standardization (ISO) certifications, *e.g.* ISO 21501-4 certification.[20] Beckman Coulter Inc. detects the coincidence in their particle counters by measuring the changes in the signal amplitude with respect to the threshold amplitude.[21] Coincidence detection is essential for accurate counting results and becomes more significant especially for counting specific target cells, *e.g.* $CD4^+$ or $CD8^+$ T lymphocytes. To diagnose HIV/AIDS and monitor the efficacy of antiretroviral therapy, $CD4^+$ and $CD8^+$ T cell counts are regularly monitored. In healthy individuals, $CD4^+$ T cell count varies from 600 to 1200 cells μL^{-1} as compared to 5000–8000 cells per microliter of leukocytes in whole blood. $CD4^+$ T cell count becomes very low (50–200 cells μL^{-1}) in AIDS patients' blood especially those who are not on active anti-retroviral drugs. In heterogeneous samples, *e.g.* blood, cell differentiation in all coincidence occurrences is essential in addition to the coincidence detection for accurate cell enumeration. Accurate counting of these specific leukocytes ($CD4^+$ and $CD8^+$ T cells) with coincidence becomes a twofold problem, first detecting a coincidence occurrence and second, differentiating a lymphocyte from other leukocytes (granulocytes and monocytes). Coincidence detection also becomes significant for erythrocyte counting from diluted whole blood.[14]

Recently, we have developed a biosensor for HIV/AIDS diagnostics based on microfluidic impedance cell counting.[22–24] We have characterized coincidence detection and cell differentiation using our cell counting biochip. Cells are counted electrically as they pass through the coplanar electrodes bonded to a 15 μm × 15 μm cross section counting channel. Erythrocytes were lysed on-chip from 10 μL of whole blood and the remaining leukocytes (lymphocytes, granulocytes and monocytes) were counted. The erythrocyte lysing reagents introduces a high amount of dilution in our sample, which results in the average time spacing between two leukocytes being 48 ms, whereas the average cell pulse width is about 0.1 ms. Even with this dilution factor, we still observe the coincidence effects in our cell counting data. In this paper, we characterized the cell coincidence occurrences into three main types based on the range of time delay at which the coincidence occurs. We have also characterized the cell differentiation in all the coincidence types. Cell differentiation becomes critically important in coincidence detection in samples with heterogeneous populations for accurate counting results.

Experimental setup and protocol

The layout of the microfluidic biochip is shown in Fig. 1a. Ten microliters of whole blood and lysing reagent at a ratio of 1 : 12 is infused at inlet ports (i) and (ii), respectively, as shown in Fig. 1a. To lyse all the erythrocytes effectively, the "lysing region" is composed of serpentine fluidic channels to provide chaotic advection to effectively mix whole blood with the lysing buffer.[22,24] Lysing of the erythrocytes change the osmolarity of the solution; thus, a quenching buffer is infused at inlet port (iii) to maintain the osmolarity and stop the lysing process to preserve remaining leukocytes.[22,24] The schematic of the experimental setup is shown in Fig. S1 and the details of the instruments used are described in the ESI.† The leukocytes are electrically counted as they pass through a counting channel of 15 μm × 15 μm cross section. The zoomed-in version of the microfabricated platinum electrodes aligned and bonded to the counting channel is also shown in Fig. 1a. The schematic of the counting channel with dimensions of 15 μm × 15 μm × 250 μm is shown in Fig. 1b (top). Three platinum electrodes of 15 μm width with 15 μm spacing are represented as A, B and C. The electronic measurement setup used to count individual cells is shown in Fig. 1b (bottom). The input signal of 5 V (rms) at 303 kHz is fed to the middle electrode B. At this frequency, cells behave as an insulating sphere and the pulse amplitude is proportional to the cell size. Z_1 and Z_2 represent the impedance change as a result of a cell passage between the A–B and B–C electrodes, respectively. 10 kΩ resistance, R, is connected to the Wheatstone bridge circuit.[24] V_1 and V_2 are unipolar signal outputs, fed to the differential amplifier to remove the common mode noise between them, thus generating a bipolar cell pulse for each passage of a cell over the electrodes. The amplitude of the bipolar pulse is proportional to the cell size. This allowed the cell differentiation based on their size. A typical bipolar voltage pulse for a lymphocyte and a granulocyte/monocyte is shown in Fig. 1c and d, respectively. The amplitude of the lymphocyte cell pulse is smaller as compared to granulocyte/monocyte. The average diameter of the lymphocytes is almost 7.8 μm,[24] thus generating smaller amplitude pulses as compared to 12 μm average cell diameter of granulocytes + monocytes. Fig. 1e shows the voltage signal acquired for 0.4 second during an experiment. Different amplitude pulses represent cells of different sizes. The maximum amplitude of all the cell pulses is recorded when it is 3 times the standard deviation of noise. The corresponding pulse peak amplitude histogram is shown in Fig. 1f. The blue dotted rectangular region represents all the leukocytes including two subpopulations, *i.e.* lymphocytes and granulocytes + monocytes. The right one represents granulocyte/monocyte population with higher pulse amplitude because of their

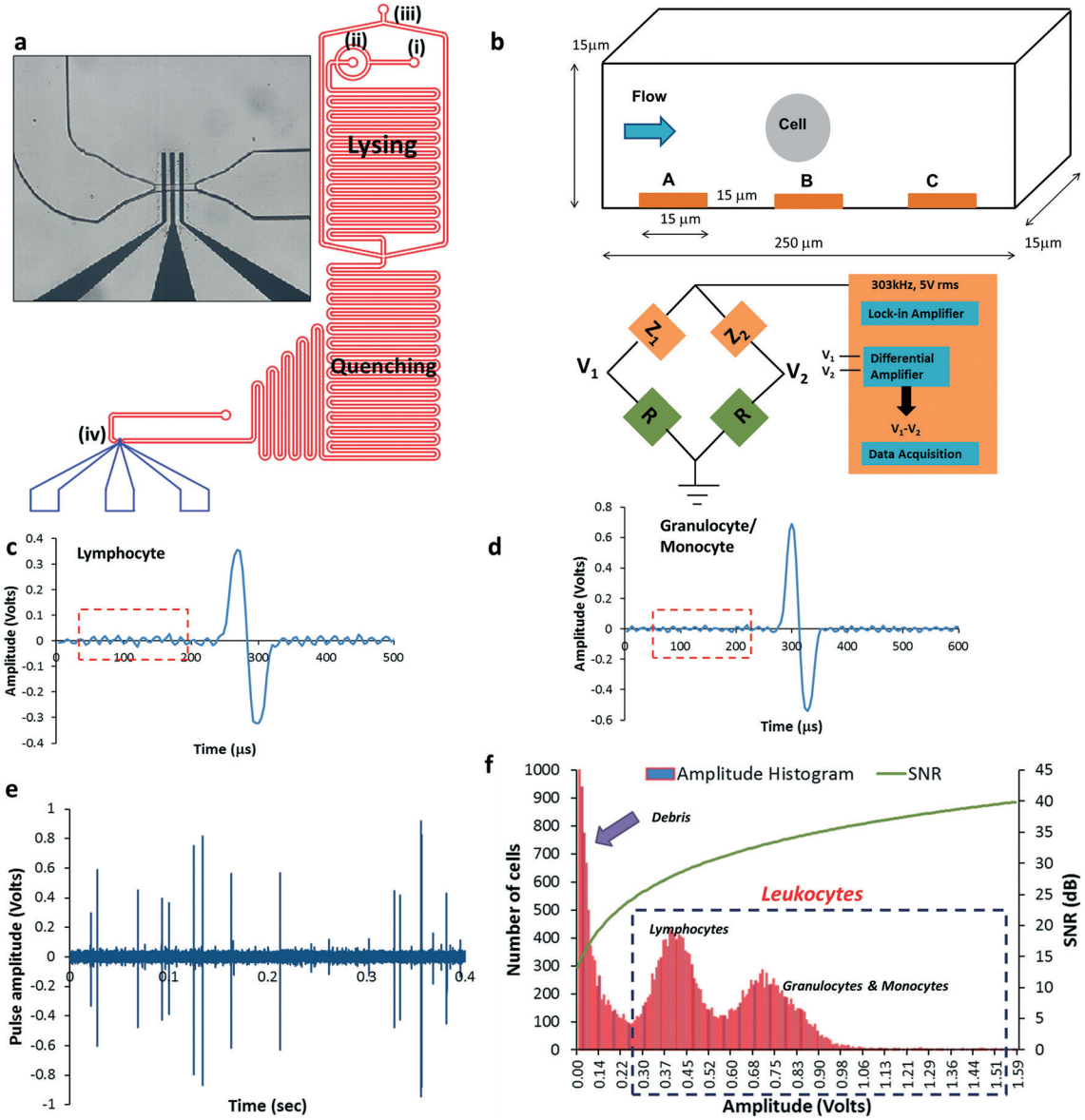

Fig. 1 Microfluidic impedance cytometer.[24] (a) Microfluidic device schematic. Blood, lysing and quenching buffers are infused at inlet ports represented as (i), (ii), and (iii), respectively. Erythrocytes are lysed as the blood gets mixed with the lysing buffer in the "lysing" region. Quenching buffer gets mixed in the "quenching" region to stop the lysing and maintain the osmolarity of the solution. The remaining leukocytes are electrically counted as they pass through a Coulter channel of 15 µm × 15 µm cross section with platinum electrodes (iv) bonded with the channel. The zoomed-in version of the electrodes with the Coulter counting channel is also shown. (b) Layout of the Coulter counting channel with dimensions of 15 µm × 15 µm × 250 µm. Platinum electrodes of 15 µm width with 15 µm spacing are represented by A, B and C (top). The electrical measurement setup to record cell pulses (bottom).[24] (c) A typical bipolar voltage pulse for a lymphocyte. (d) A typical bipolar pulse for a granulocyte/monocyte. (e) The bipolar pulses are produced for each cell passage with its amplitude proportional to the cell size. The data show electrical cell pulses recorded for 0.4 second. (f) The peak amplitude of all the pulses is recorded above 3 times the standard deviation of noise. The corresponding pulse peak amplitude histogram is shown. The blue dotted rectangular region represents all the leukocytes including two populations, *i.e.* lymphocytes and granulocytes + monocytes. To the left of the leukocyte population is erythrocyte debris, and the rectangular region is selected by considering the minima between them. Signal-to-noise ratio (SNR) is also shown on a histogram for all the cells and is found by calculating the root-mean-square (rms) value of the respective voltage pulses and the rms of the noise for 150 samples as represented by black dotted rectangular regions in (c) and (d).

larger size. To the left of the leukocyte population is erythrocyte debris, and the rectangular region is selected by considering the minima between erythrocyte debris and leukocyte population. Signal-to-noise ratio (SNR) is found by calculating the root-mean-square (rms) value of the electrical cell pulses and the rms of the noise for 150 samples shown by black dotted rectangular regions in Fig. 1c and d. The SNR value for each cell is computed for both lymphocytes and granulocytes/monocytes and is also shown on a histogram in Fig. 1f.

Results

Cell pulse modelling and simulation

A simple approximation of an experimental bipolar cell pulse as a sinusoid shows a large variation between simulated and experimental cell pulse as shown in Fig. S2a.† A bipolar electrical voltage pulse generated for each passage of a cell over the electrodes is a result of a differential signal of two unipolar pulses. As a cell moves over the electrodes, it generates a unipolar pulse from A to C and from B to D as shown by blue lines in Fig. 2a. The resulting differential signal for a lymphocyte and a granulocyte/monocyte is shown in Fig. 1c and d, respectively. We modelled the cell pulse by using the following mathematical function:

$$\text{Cell pulse} = \begin{cases} A_u \sin t, & 0 \geq t \leq \dfrac{3T}{5} \\ -A_d \sin(t - \dfrac{2T}{5}), & \dfrac{2T}{5} \geq t \geq T \end{cases} \quad (1)$$

where T is the time a cell takes to move from A to D, equivalent to bipolar pulse width. The cell pulse from A to C is modelled as $A_u \sin t$ and from B to D as $A_d \sin\left(t - \frac{2T}{5}\right)$, with A_u and A_d being the respective signal amplitudes. The resulting differential signal, a bipolar pulse, is shown in red. Cell pulse is simulated using modelling eqn (1) and compared with the experimental electrical cell pulse as shown in Fig. S2b.† The difference between the negative peak amplitudes of the experimental and the simulated cell pulses shows that the absolute negative peak amplitude of the electrical cell pulse is slightly smaller than (almost 0.9 times) the positive peak amplitude as discussed in our earlier study.[24] Taking this into account, cell pulse is simulated again using the modelling eqn (1) and compared with the experimental electrical cell pulse in Fig. 2b. The difference between the experimental and simulated cell pulses shows that the impedance starts to change earlier than position A and ends after position D. This happens as the electric field lines extend beyond points A and D; however, the electric field strength is small, thus producing a small impedance change. We estimated this time difference to be $T/20$ as shown in Fig. 2c. The cell pulse is simulated after incorporating $T/20$ time difference and compared with the experimental electrical cell pulse as shown in Fig. 2d. This gives the fair approximation of the simulated cell pulse with the experimental electrical cell pulse.

Definition of types of cell coincidences

Coincidence detection is essential for accurate cell counting. In the case of different cell types, it is not only important to identify that a coincidence occurs but also to differentiate between different cell types. We have characterized the coincidence into three types based on the time delay at which the second cell appears in the detection area, *i.e.* $T/20$ time before position A as shown in Fig. 2c. Type 1 is defined for the range of $\left(0 \text{ to } \frac{6T}{20}\right]$, type 2 for $\left(\frac{6T}{20} \text{ to } \frac{13T}{20}\right]$, and type 3 for $\left(\frac{13T}{20} \text{ to } T\right]$ (Fig. 3). The ranges for the above types are

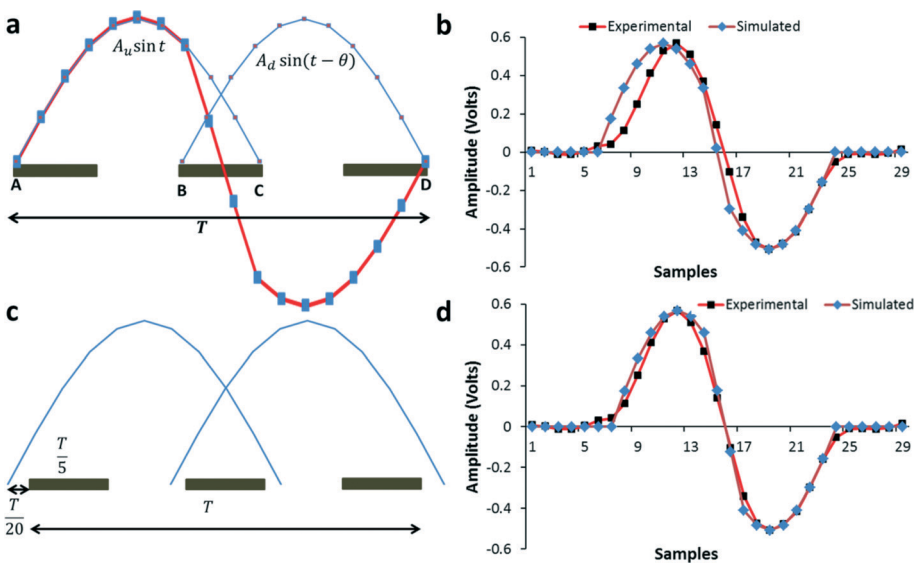

Fig. 2 Modelling of the electrical cell pulse. (a) As a cell moves over the electrodes, it generates a unipolar pulse from A to C and from B to D as shown by the blue curves. The electrical pulse from A to C is modelled as $A_u \sin t$ and from B to D as $A_d \sin(t - \theta)$ with A_u and A_d being the signal amplitudes and $\theta = \frac{2T}{5}$. The resulting differential signal, a bipolar pulse, is shown in red. T is the time a cell takes to move from A to D, equivalent to pulse width. (b) The experimental and simulated electrical pulses with a cell model as represented in (a) are shown. (c) The difference between the experimental and the simulated cell pulses suggests that the impedance starts to change earlier than position A and end after position D by time equal to $T/20$. (d) A comparison of the simulated and experimental electrical cell pulses while considering the cell model as given in (c) is shown.

selected to categorize and facilitate the differentiation between the coincidence cells.

Type 1 cell coincidence characterization. Type 1 cell coincidence occurs when the second cell enters the detection area within the time delay range of $\left(0 \text{ to } \frac{6T}{20}\right]$, resulting in increased pulse amplitude and pulse width. The pulse width increases by an amount equal to the time delay at which the cell coincidence occurs and is represented as $\text{Width}_{\text{coin}} = \text{Width}_{\text{no-coin}} + \varnothing$, where $\varnothing$ is the time delay at which the second cell enters the detection region. The increase in the amplitude of the cell pulse can be seen by measuring the slope of the cell pulse. Fig. 4a shows the simulated cell pulse and its corresponding change in slope. During the range of type 1 coincidence, *i.e.* $\left(0 \text{ to } \frac{6T}{20}\right]$, the slope is decreasing. In the case of a cell coincidence at a time delay of $3T/20$, the resulting simulated cell pulse is shown in Fig. 4b. As the second cell enters the detection area, there is a sharp increase in amplitude indicated by a blue arrow at the point of coincidence. This sharp increase in the cell pulse amplitude at the point of coincidence, *i.e.* $3T/20$, results in the sudden increase in slope at the corresponding coincidence point. An example of type 1 coincidence is shown in Fig. 4c where an experimental cell coincidence is shown as indicated by the increase in pulse amplitude and the pulse slope at the point of coincidence.

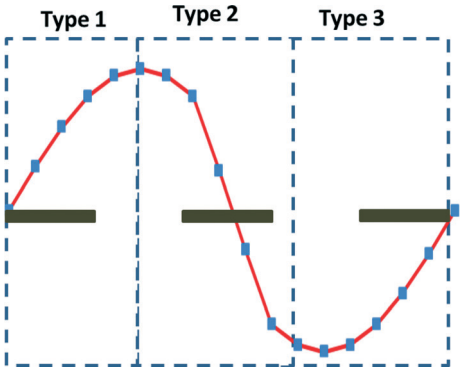

Fig. 3 Coincidence types characterization. Three types of cell coincidences were defined based on the time delay of the second cell appearance. Type 1 is defined for the range of $\left(0 \text{ to } \frac{6T}{20}\right]$, type 2 for $\left(\frac{6T}{20} \text{ to } \frac{13T}{20}\right]$, and type 3 for $\left(\frac{13T}{20} \text{ to } T\right]$, respectively. The range for the types is selected based on differentiating the coincidence cells.

Differentiating the individual cell types with their corresponding peak cell pulse amplitudes from the coincidence signal is essential for accurate cell counting. Type 1 coincidence results in increased amplitudes of the positive and negative peaks of the coincident cell pulse. The increase in the amplitude of the positive peak of the coincident cell pulse with varying coincidence time delay values is shown in Fig. S3.† The peak amplitude of the coincident cell pulse is given by

$$A_1 + \sin(t_0)A_2 \quad (2)$$

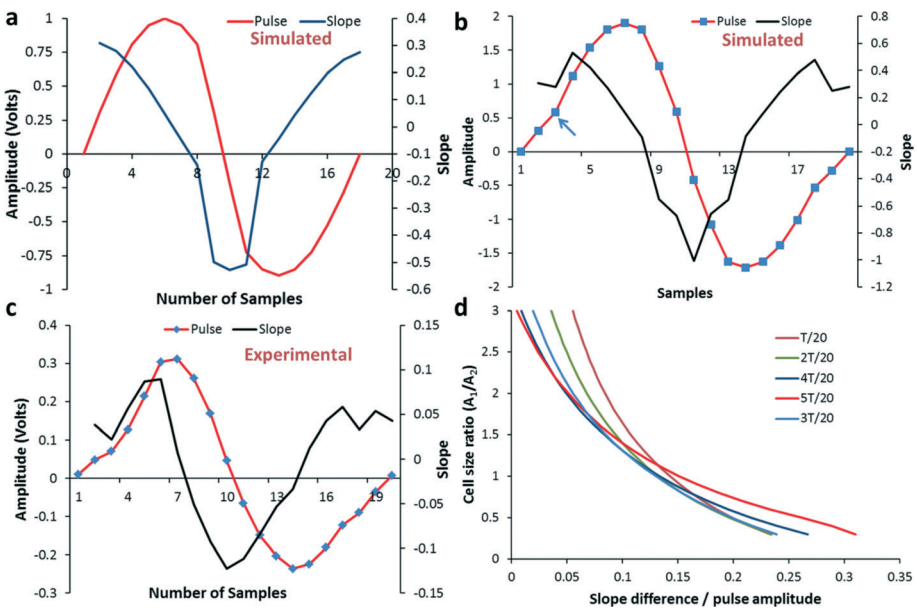

Fig. 4 Type 1 cell coincidence characterization. (a) The simulated cell pulse and its corresponding change in slope are shown. (b) In the case of a cell coincidence at $3T/20$, the resulting simulated cell pulse is shown. As the second cell enters the detection area, there is a sharp increase in amplitude indicated by a blue arrow at the point of coincidence. The sharp amplitude increase results in a sharp increase in slope at the corresponding point of coincidence. (c) Experimental cell coincidence is shown as indicated by the increase in pulse amplitude and the pulse slope at the point of coincidence. (d) The simulated ratio of the slope difference to the pulse peak amplitude is plotted w.r.t. different values of the cell size ratios (A_1/A_2) for the whole range of coincidence time delays for type 1 coincidence. A_1 is the pulse amplitude proportional to the size of the first cell and A_2 is the pulse amplitude proportional to the size of the second cell. This can be used to differentiate the individual pulse amplitude from the resulting coincidence pulse.

where A_1 and A_2 are the peak amplitudes of the first and second coincident cell pulses, respectively. t_0 is the point of time delay at which coincidence occurs, which can be determined by finding the point during $\left(0 \text{ to } \frac{6T}{20}\right]$ at which the decreasing slope of the corresponding cell pulse starts increasing. We have simulated the ratio of the slope difference (at the coincidence point) to the coincident pulse peak amplitude and plotted w.r.t. different values of the cell size ratios (A_1/A_2) for the whole range of type 1 coincidence $\left(0 \text{ to } \frac{6T}{20}\right]$ as shown in Fig. 4d. A_1 is the pulse amplitude proportional to the size of the first cell and A_2 is the pulse amplitude proportional to the size of the second cell. After finding the ratio of the change in the slope at coincidence point to the peak amplitude of the coincidence pulse, Fig. 4d can be used to find the value of A_1/A_2 by looking at the corresponding coincidence time plot. The value of A_1/A_2 along with eqn (2) can be used to differentiate the individual pulse amplitudes of coincidence cells from the resulting coincident cell pulse.

Type 2 cell coincidence characterization. Type 2 cell coincidence occurs when the second cell enters the detection area within the time delay range of $\left(\frac{6T}{20} \text{ to } \frac{13T}{20}\right]$. The coincidence pulse width increases by an amount equal to the time delay at which the cell coincidence occurs and is given as $\text{Width}_{\text{coin}} = \text{Width}_{\text{no-coin}} + \varnothing$, where $\varnothing$ is the time delay at which the second cell enters the detection region. However, there is no increase in the amplitude of the first positive peak of the coincident pulse for the range of $\left(0 \text{ to } \frac{6T}{20}\right]$. The amplitude of the first positive peak represents the peak pulse amplitude of the first cell irrespective of the coincidence time delay as by the time at which the first positive peak appears the second cell has not yet entered the detection area. The amplitude of the last negative peak represents the negative pulse amplitude of the second cell irrespective of the coincidence time delay as by the time the last negative peak appears the first cell has already left the detection area. The first positive peak and last negative peak differentiate both cells. Fig. 5a shows the simulated cell pulses when the second cell that is equal to the size of the first cell $(A_2 = A_1)$ enters the detection region for the entire time delay range. The 1st cell and the 2nd cell are represented by the first positive and the last negative peak amplitudes, respectively, as indicated by arrows in Fig. 5a. The blue dotted region in Fig. 5a represents the region in which the signal is the result of the coincidence of both cells. To the left of the dotted

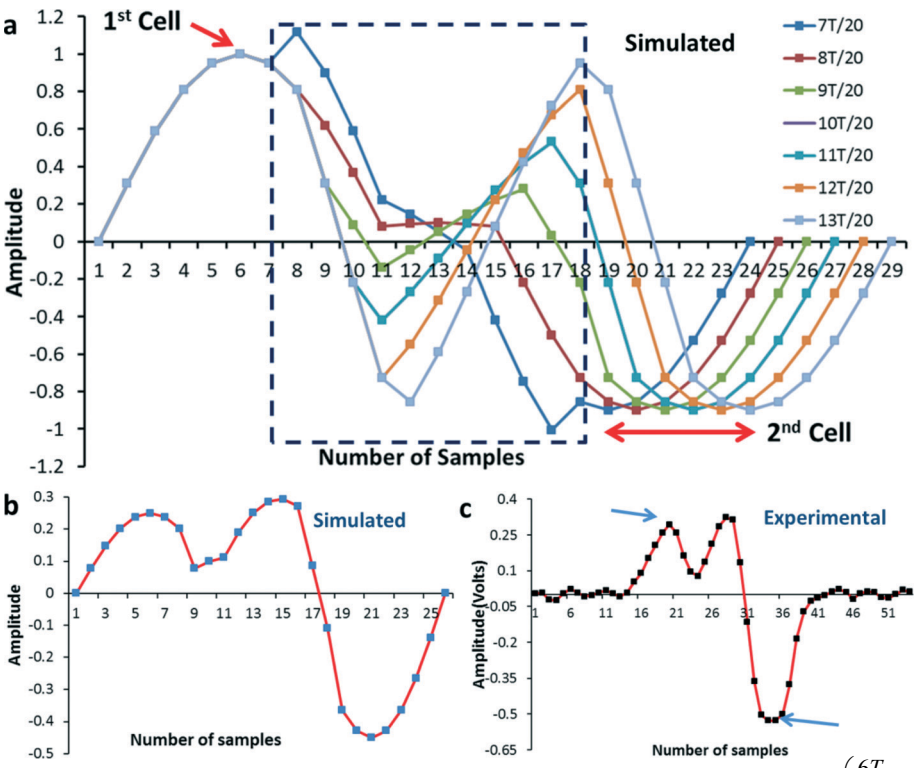

Fig. 5 Type 2 cell coincidence occurs when a second cell enters the detection area with a time delay in the range of $\left(\frac{6T}{20} \text{ to } \frac{13T}{20}\right]$. (a) The simulated cell pulses for the entire time delay range of type 2 coincidence when the second cell that is equal to the size of the first cell $(A_2 = A_1)$ enters the detection region. (b) The simulated cell pulse when the second cell that is twice the size of the first cell $(A_2 = 2A_1)$ enters the detection region with a time delay of 9T/20. (c) The experimental electrical cell pulse as a result of type 2 coincidence with blue arrows showing the peak amplitudes to be considered for cell differentiation.

region is the signal generated purely as a result of the first cell's entrance into the detection region, and to the right of the dotted rectangle is the signal generated as a result of only the second cell's exit from the detection region. Fig. S4† shows the simulated cell pulses when the first cell that is twice the size of the second cell ($A_1 = 2A_2$) enters the detection region for the entire time delay range. Similarly, Fig. S5† shows the simulated cell pulses when the second cell that is twice the size of the first cell ($A_2 = 2A_1$) enters the detection region for the entire time delay range. Fig. 5b shows the simulated cell pulses when the second cell that is twice the size of the first cell ($A_2 = 2A_1$) enters the detection region with a time delay of $9T/20$. The corresponding experimental electrical cell pulse as a result of type 2 coincidence is shown in Fig. 5c. The blue arrows at the first positive peak and last negative peak show the peak amplitudes to be considered for cell differentiation. The amplitude profile between the first positive peak and the last negative peak depends on the coincidence time delay and the individual pulse amplitudes of both cells. However, differentiating both cells only depends on the first positive and the last negative peak and is independent of the amplitude profile in the middle.

Type 3 cell coincidence characterization. Type 3 cell coincidence occurs when the second cell enters the detection area within the time delay range of $\left(\frac{13T}{20} \text{ to } T\right]$. During this range of coincidence time delay, both cells can be identified by the first and second positive peak amplitudes. In type 3 coincidence, the positive peak amplitude of the second pulse remains the same irrespective of the time delay at which coincidence occurs. We have simulated the cell pulses when the second cell that is equal to the size of the first cell ($A_2 = A_1$) enters the detection region for the entire time delay range of $14T/20$ to T as shown in Fig. 6a. As shown in Fig. 6a, the first positive peak remains the same irrespective of the coincidence time delay. The occurrence of the second positive peak associated with the second cell depends on the time delay at which the second cell enters the detection region; however, its amplitude is independent of the coincidence time delay for type 3 coincidence. The second positive peak amplitude is proportional to the size of the second cell. Therefore, the first cell can be identified by measuring the amplitude of the first positive peak and the second cell by measuring the amplitude of the second positive peak. The experimental electrical cell pulse when the second cell that is slightly smaller than the first cell enters the detection region with a time delay of $18T/20$ is shown in Fig. 6b.

Multiple coincidence: combination of the different coincidence types

Multiple coincidences occur when multiple cells enter the detection region during different time delays while generating a single electrical cell pulse. For example, we have simulated a multiple-coincidence-type case, when the second cell that is half the size of the first cell enters the detection area with a time delay of $4T/20$. The third cell (that is equal to the size of the first cell) follows and enters the detection area with a time delay of $8T/20$ with respect to the first cell. The resulting simulated cell pulse which is a combination of type 1 and type 2 coincidences is shown in Fig. 7a. The corresponding experimental cell pulse is shown in Fig. 7b.

Accurate $CD4^+$ T cell enumeration with coincidence detection. We have shown that specific leukocytes, *e.g.* $CD4^+$ or $CD8^+$ T cells, can be enumerated by counting all the leukocytes after quenching at the first electrical cell counter.[18] Then, the $CD4^+$ or $CD8^+$ T cells are captured by their specific cell antibody adsorbed in a capture chamber with PDMS pillars to increase the capture efficiency (Fig. 8). The second counter at the exit of the capture chamber counts the remaining cells after capture. $CD4^+$ and $CD8^+$ T cells are a subtype of lymphocyte population, and the difference in lymphocyte cell populations from both counters gives the number of captured $CD4^+$ or $CD8^+$ T cells. Accurate counting of these specific leukocytes with coincidence becomes a twofold problem, first detecting a coincidence occurrence and second differentiating a lymphocyte from a granulocyte + monocyte. The biochip's size is 3 cm × 4 cm and is shown in Fig. 8b.[22]

Blood samples from healthy donors and HIV-infected patients were collected for this study. $CD4^+$ and $CD8^+$ T cell

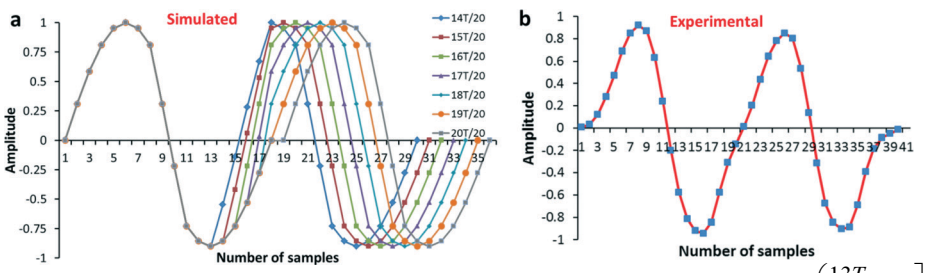

Fig. 6 Type 3 cell coincidence when a second cell enters the detection area with a time delay in the range of $\left(\frac{13T}{20} \text{ to } T\right]$. (a) The simulated cell pulses when the second cell that is equal to the size of the first cell ($A_2 = A_1$) enters the detection region for the entire time delay range of $14T/20$ to T. In type 3 coincidence, the positive peak amplitude of the second pulse remains the same irrespective of the time delay at which the coincidence occurs. The positive peak amplitudes of both pulses are considered for cell differentiation. (b) The experimental electrical cell pulse when the second cell enters the detection region with a time delay of $18T/20$.

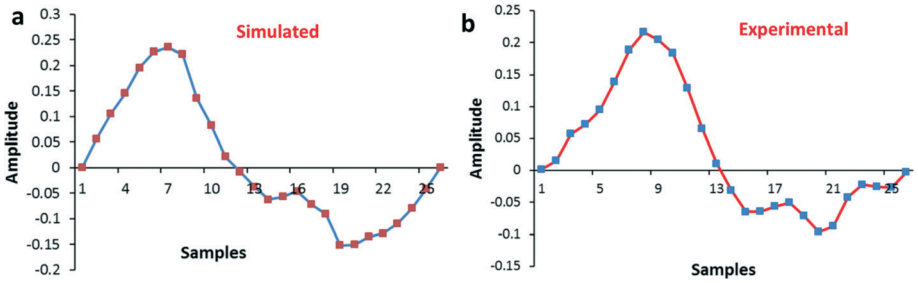

Fig. 7 Combination of different coincidence types. (a) The simulated coincidence cell pulse when the second cell that is half the size of the first cell enters the detection area with a time delay of 4T/20 and when the third cell (that is equal to the size of the first cell) enters the detection area with a time delay of 8T/20 w.r.t. the first cell. (b) The experimental cell pulse with a combination of coincidence types 1 and 2.

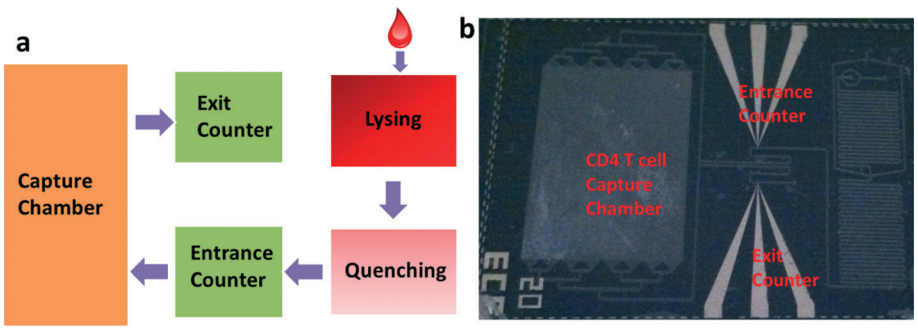

Fig. 8 (a) The flow layout of the biochip to enumerate CD4 T cell from whole blood. After the blood infusion and lysing/quenching module, the entrance counter counts all the leukocytes. CD4 T cells are depleted in the capture chamber and the remaining cells are counted by the exit counter. The difference in lymphocytes count between two counters gives the number of captured $CD4^+$ or $CD8^+$ T cells.[22] (b) The picture of the actual biochip adapted from ref. 22. The size of the biochip is 3 cm × 4 cm.

count is done with and without coincidence detection at both counters. Fig. 9 shows the comparison between $CD4^+$ T cell counts (n = 10 healthy, n = 10 HIV infected) from our biochip and the flow cytometer from Carle Foundation Hospital (Urbana, IL) with and without coincidence detection. Counting the cells with coincidence detection shows a high correlation with a perfect slope ($y = 1x$, $R^2 = 0.99$) compared to cell counts without coincidence detection ($y = 0.95x$, $R^2 = 0.96$). This improvement in counting results is reflected by the increase in the slope of the linear line comparing the biochip and the control counts from 0.95 (without coincidence) to 1.0 (with coincidence) as shown in Fig. 9a, which ideally should be 1 for a perfect correlation. In order to see the difference more clearly, Bland–Altman analysis is also used to compare the biochip counts with flow cytometry control counts. A negative bias of 37 cells μL^{-1} shows that our biochip is counting, on average, 37 $CD4^+$ T cells μL^{-1} less than the control counts without coincidence detection cell counting as shown in Fig. 9b. $CD4^+$ T cell counting with coincidence detection results in a bias value of about 4 cells μL^{-1} as shown in Fig. 9c. Fig. 9d shows the comparison between $CD8^+$ T cell counts (n = 10 healthy, n = 10 HIV infected) from our biochip and the flow cytometer from Carle Foundation Hospital (Urbana, IL) with and without coincidence detection. Counting the $CD8^+$ T cells with coincidence detection shows a high correlation with a greater slope ($y = 0.98x$, $R^2 = 0.96$) as compared to cell counts without coincidence detection ($y = 0.93x$, $R^2 = 0.96$). A positive bias of 55 cells μL^{-1} shows that our biochip is counting, on average, 55 $CD8^+$ T cells μL^{-1} greater than the control counts without coincidence detection as shown in Fig. 9e. $CD8^+$ T cell counting with coincidence detection results in a negative bias value of 19 cells μL^{-1} as shown in Fig. 9f. The average % error in $CD4^+$ T cell count is reduced from 8.2% (without coincidence) to 5.6% (with coincidence). Similarly, average % error in $CD8^+$ T cell count is reduced from 7.9% (without coincidence) to 5.5% (with coincidence) as shown in Fig. 10.

Erythrocyte counting in diluted blood with coincidence detection. The probability of coincidence (P) as a function of sample concentration (λ), sensing volume (τ) and the number of the coincidences is given by the following equation:

$$P_k(\tau) = \frac{e^{-\lambda\tau}(\lambda\tau)^k}{k!}. \quad (3)$$

The number of coincidences can be minimized by reducing the sample concentration and the sensing region.[18] Erythrocytes are the most highly concentrated type of cell in the blood and will result in more coincidence occurrences. We have shown the probability of erythrocyte coincidence (k = 2) with varying dilution factors when whole blood is diluted with PBS in Fig. 11(a) using eqn (3). The sensing region is about 16.9 pL. The coincidence probability decreases significantly from 15.3% to 1.2% as the dilution factor is increased from 100 to 500. However, increased dilution factor also results in using more reagent volume and increased experiment time.

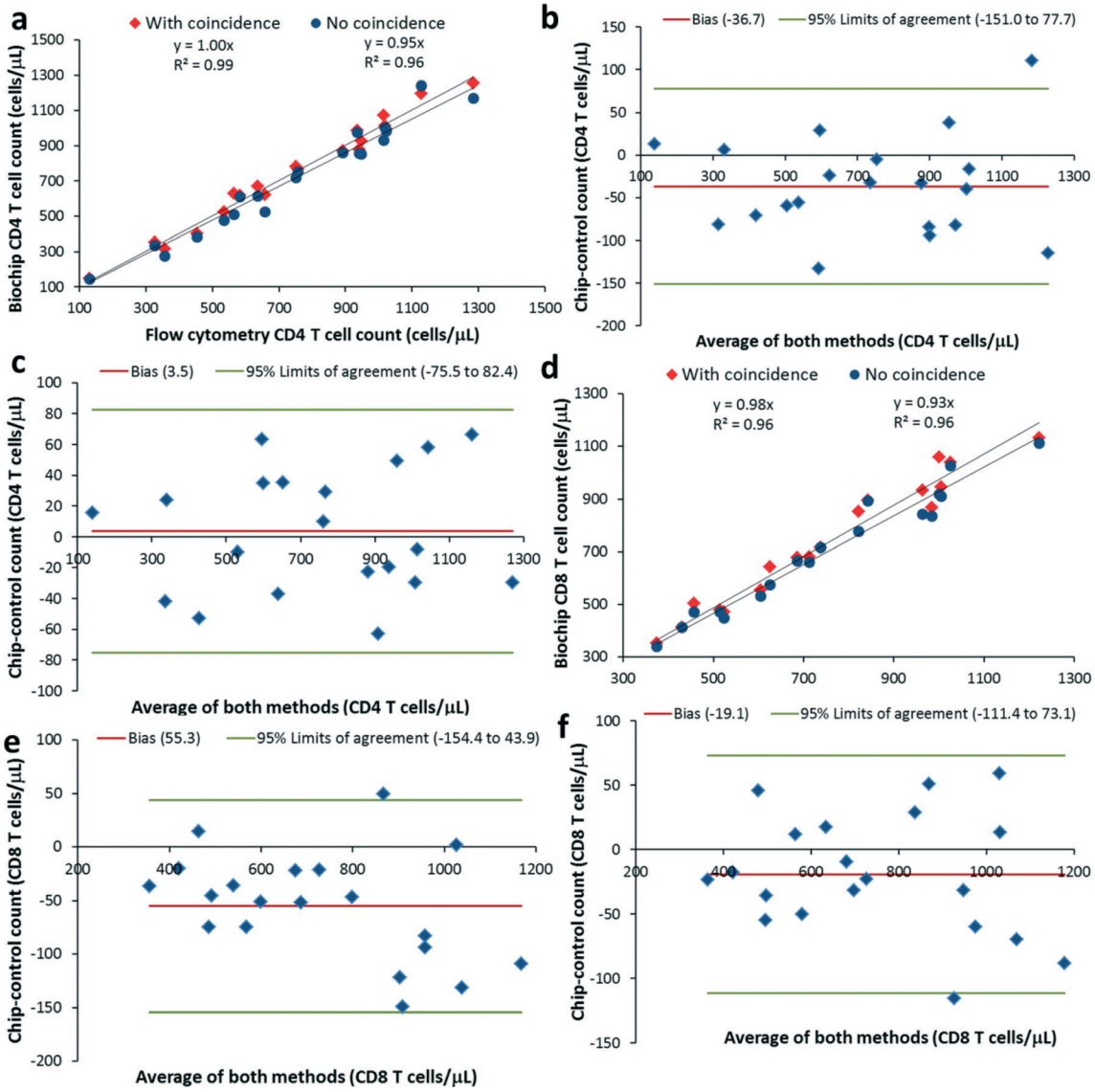

Fig. 9 (a) $CD4^+$ T cell comparison (n = 20) with and without coincidence detection with flow cytometry control measurements from Carle Foundation Hospital. (b) Bland–Altman plot to compare CD4 T cell count without coincidence detection. (c) Bland–Altman plot to compare CD4 T cell count with coincidence detection. (d) $CD8^+$ T cell comparison (n = 20) with coincidence detection and without coincidence detection with the flow cytometry control from Carle Foundation Hospital. (e) Bland–Altman plot to compare CD8 T cell count without coincidence detection. (f) Bland–Altman plot to compare CD8 T cell count with coincidence detection.

Fig. 11(b) shows the comparison of erythrocyte counts as measured from the biochip and from flow cytometry with varying dilution factors. Erythrocyte counting with coincidence detection incorporated in the analysis results in a high correlation coefficient and a slope of the linear line closer to unity (R^2 = 0.99, y = 0.94x) as compared to without coincidence detection (R^2 = 0.97, y = 0.81x). Thus, erythrocyte counting with coincidence provides more accurate counting results, especially at lower dilution factors.

Discussion

In our current study, we have used the three-coplanar electrode design which comprises the cell detection region of 75 μm. Reducing the length of the detection region will decrease the instances of the coincidences. The length of the detection region can be reduced by decreasing the width and spacing of the electrodes. This will result in reduced pulse width and will require higher sampling rates to get optimum resolution (number of samples) in each cell pulse for accurate coincidence detection. Fig. S6† shows that the required sampling rate for optimum resolution in cell pulse decreases linearly (R^2 = 0.92) and the pulse width increases linearly (R^2 = 1) with an increase in the width and spacing of electrodes from 5 to 15 μm. Although the reduced length of the detection region decreases the coincidence occurrence, it will require higher sampling rates, resulting in higher memory and processing speed requirements for accurate cell counting.

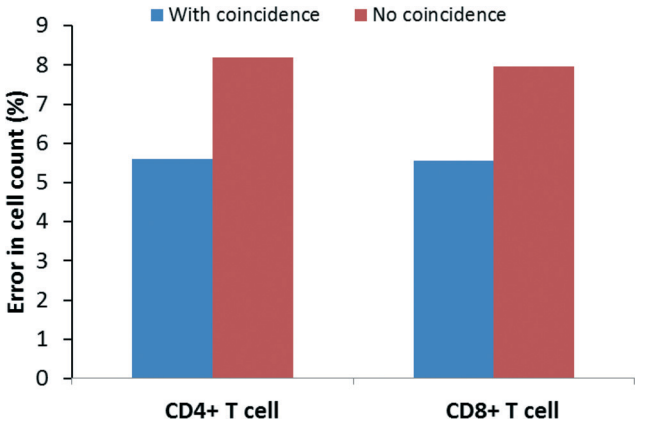

Fig. 10 The average % error in $CD4^+$ T cell count is reduced from 8.2% (without coincidence) to 5.6% (with coincidence). The average % error in $CD8^+$ T cell count is reduced from 7.9% (without coincidence) to 5.5% (with coincidence).

We have also shown the coincidence probability change with varying width and spacing of the electrodes in Fig. S7.† The probability decreases linearly as the width and electrode spacing is reduced. The secondary axis shows the corresponding sensing volume. The fabrication of electrodes with reduced width and spacing also result in jagging effects on the edges of the electrodes which can potentially affect the signal-to-noise ratio. The roughness of the edges can be minimized by using the effective hard contact with vacuum while doing photolithography. Coincidence detection and cell differentiation requires extra data processing for type 1 as compared to type 2 or type 3. In real-time data processing, the cell pulse data need to be stored and then processed to find the coincidence time delay from the slope of the cell pulse and then further used to differentiate between individual cells. However, cell differentiation in type 3 coincidence does not require extra data processing as both cells can be identified from positive peak amplitudes automatically with regular cell counting.

Multiple coincidences for the same type are negligible. More than 2 cells can never be present in any one of the coincidence region as the size of the coincidence region is almost 19, 26 and 30 μm for coincidence types 1, 2 and 3, respectively; however, the size of a typical leukocyte is about 8–12 μm, depending on the subtype of leukocyte. In other particle counting applications with size distribution much smaller than the coincidence region, the multiple coincidence of the same type can occur. However, in cell counting applications, like in CD4 and CD8 T cell count (for AIDS patients) from whole blood, the current coplanar electrode design is optimum to perform coincidence detection and individual cell differentiation for accurate cell counting. Our current system allows the occurrence of multiple coincidences of different types, as the size of the sensing region is almost 75 μm, and more than 2 cells can be present in the sensing region. The occurrence of multiple coincidence would effectively be eliminated by reduced sensing region (using smaller electrode width and spacing), resulting in no more than 2 cells present at the same time in the sensing region. However, a more detailed characterization for multiple coincidences is needed with a larger sensing region or counting smaller particles for other cell counting applications. The coincidence of more than 2 cells would introduce more types of impedance pulse spectra, making individual cell identification more difficult. In real-time applications, this would also require more enhanced data processing.

Introducing large dilutions can also minimize the coincidence occurrences. In our case of specific WBC counting, the blood sample is lysed and quenched, and the dilution factor is limited by the optimized lysing of all erythrocytes. Changing the dilution factor would result in different lysing and quenching effects on the erythrocytes and remaining leukocytes. Thus, we cannot provide large dilutions, as we are limited by lysing/quenching effects. This makes the real-time detection of the cell coincidences and their differentiation necessary for accurate cell counting. Accurate counting of $CD4^+$ or $CD8^+$ T cell from our biochip also depends on other factors including the efficiency of erythrocyte lysing, preserving leukocytes, and capture efficiency of $CD4^+$ and $CD8^+$ T cells. However, cell counting with coincidence detection results in improved counting accuracy and a better correlation with control counts as shown in Fig. 9.

As the need for utilizing coincidence detection will be higher for samples with larger number of cells, we applied the technique to counting of RBCs, especially with varying dilutions. Whole blood will result in clogging and too many coincidences to produce any useful results. As we vary the blood : PBS dilution from 1 : 100 to 1 : 500, we see the importance of the coincidence detection most evident at the lower

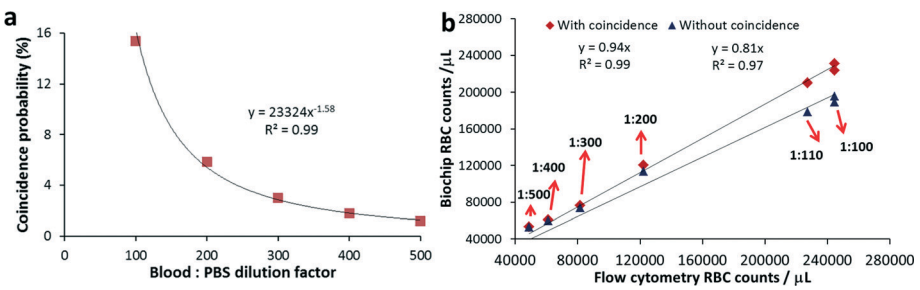

Fig. 11 (a) The coincidence probability of erythrocyte counts with varying dilution factors when whole blood is diluted with PBS. (b) The comparison of erythrocyte counts with controls with varying blood : PBS dilution factors (*e.g.* 1 : 500). Erythrocyte counting with coincidence detection provides increased accuracy in the counting results.

dilutions as expected. At 1 : 100, we see a significant improvement as the % cell counting error is reduced from 20.5% (without coincidence detection) to 5.5% (with coincidence detection). Although at high dilution factors coincidence occurrences would be less, but it will require increased reagent volume and also increased assay time. Having a sensitive coincidence detection system in a cell counter would be more useful especially for PoC applications where time of assay and costs are the limiting factors.

The cell counting experiment time is about 30 minutes. For PoC applications, this would be suitable. However, with further optimization of the biochip, we believe that we can perform the cell counting assay in less than 15 minutes. This can be done by increasing the total flow rate while keeping the optimized lysing time, quenching time and shear stress for cell capture constant. Lysing and quenching times can be kept constant by changing the height of the lysing/quenching channels. Increasing the flow rate will also result in different shear stress for the cell capture. In order to get the same shear stress at high flow rates, the height of the capture chamber will be increased and optimized to get the same capture efficiency.

Conclusions

Coincidence detection is very essential for accurate counting results especially for samples with small concentration of target cells. In heterogeneous samples, *e.g.* blood, cell differentiation in all the coincidence occurrences is essential in addition to the coincidence detection for accurate cell enumeration. In this paper, we have characterized the coincidence detection with cell differentiation using our microfluidic impedance cytometer. We have determined an approximate mathematical model to simulate the electrical cell pulse and its coincidences. We show that coincidence detection can be characterized into three main types based on the range of time delay at which the cell coincidence occurs. We have characterized the cell differentiation in all the coincidence types. We also demonstrate the multiple coincidences of different types. We further used healthy and HIV-infected patient blood samples to count the $CD4^+$ and $CD8^+$ T cells and have shown that the cell counting with coincidence detection gives more accurate results than cell counting without coincidence detection.

Materials and methods

Chip fabrication

The negative of electrodes is patterned on a 4-inch glass wafer using an LOR2A (Microchem Corp.) and an S-1805 (Rohm and Haas Electronic Materials), exposed, and further developed using a CD-26 developer.[22–24] 75 nm Pt conduction layer is evaporated after 25 nm Ti as adhesion layer on the glass substrate using an SEC-6000 evaporator (CHA Industries). Microchem Remover PG is used to lift off the undesired metal. The fluidics layer (lysing, quenching, counting channels) is created by patterning an SU-8 50 negative photoresist on a Si wafer as a negative master. A base mixture having a polydimethylsiloxane (PDMS)-to-curing agent ratio of 10 : 1 is used and was poured and then cured for 15 minutes at 150 °C to create the microfluidic channels.[22,24] PDMS and an electrode chip were aligned and permanently bonded by exposing them to oxygen plasma for 1 minute.

Blood sample acquisition

The blood samples from healthy donors used in this study were collected from University of Illinois student volunteers through a consent process approved by the Institutional Review Board (IRB). Blood was drawn *via* venipuncture and collected in EDTA-coated BD vacutainers (BD Biosciences), which were kept on a rotisserie at room temperature. Experiments were performed immediately after the blood draw. Blood samples from HIV-infected patients were collected from the Champaign-Urbana public health district through a consent process approved by the IRB. Samples were brought to the Micro and Nanotechnology Laboratory at the University of Illinois at Urbana-Champaign for $CD4^+$ T cell counting.

Reagents

The composition of the lysing reagent used for lysing erythrocytes in the blood is 0.12% (v/v) formic acid and 0.05% (w/v) saponin in DI water. The composition of the quenching buffer is concentrated phosphate buffer saline (PBS) and 0.6% (w/v) sodium carbonate in DI water.[22,24]

$CD4^+$/$CD8^+$ cell capture

$CD4^+$ and $CD8^+$ T cells are captured by immobilizing their respective antibodies in the capture chambers. Purified mouse antibody to human CD4 (clone 13B8.2; IM0398, Beckman Coulter, Inc., Brea, CA) and purified mouse antibody to human CD8 (clone 3B5; MHCD0800, Life Technologies, NY) are immobilized by adsorption surface chemistry.

Acknowledgements

The authors would like to acknowledge the help of Gregory Damhorst for the blood draw from healthy human donors, Lara Orlandic for help in fabricating microfluidic devices, and Gary Durack, Founder of iCyte, and Aneeq Zaman for useful discussions. Funding: R. B. acknowledges the support of the NSF NSEC through OSU grant number EEC-0914790 and funding from the University of Illinois, Urbana-Champaign.

References

1 W. H. Coulter, *US Pat.*, 2,656,508, 1953.
2 H. A. Teass, J. Byrnes and A. Valentine, *Tech. Q. – Master Brew. Assoc. Am.*, 1998, 35, 101–103.
3 L. W. Phipps and F. H. S. Newbould, *J. Dairy Res.*, 1966, 33, 51–64.
4 Z. Zhang, J. Zhe, S. Chandra and J. Hu, *Atmos. Environ.*, 2005, 39, 5446–5453.

5 R. DeBlois and R. K. Wesley, *J. Virol.*, 1977, **23**, 227–233.
6 J. J. Kasianiwicz, E. Brandin, D. Branton and D. W. Dreamer, *Proc. Natl. Acad. Sci. U. S. A.*, 1996, **93**, 13770–13773.
7 O. A. Saleh and L. L. Sohn, *Proc. Natl. Acad. Sci. U. S. A.*, 2003, **100**, 820–824.
8 F. Arqueros, F. Blanco and B. J. Cisneros, *Eur. J. Phys.*, 2004, **25**, 399–407.
9 W. L. Leo, *Techniques for Nuclear and Particle Physics Experiments*, Springer, Berlin, 1994.
10 R. Kauffman, *Transactions of Society of Tribologists and Lubrication Engineers*, 1989, **45**, 147–153.
11 T. Sun and H. Morgan, *Microfluid. Nanofluid.*, 2010, **8**, 423–443.
12 D. Holmes, D. Pettigrew, C. Reccius, J. D. Gwyer, C. Berkel, J. Holloway, D. E. Davies and H. Morgan, *Lab Chip*, 2009, **9**, 2881–2889.
13 K. C. Cheung, M. Di Berardino, G. S. Kampmann, M. Hebeisen, A. Pierzchalski, J. Bocsi, A. Mittag and A. Tarnok, *Cytometry, Part A*, 2010, **77**, 648–666.
14 C. Berkel, J. D. Gwyer, S. Deane, N. Green, J. Holloway, V. Hollis and H. Morgan, *Lab Chip*, 2011, **11**, 1249.
15 D. Holmes and H. Morgan, *Anal. Chem.*, 2010, **82**, 1455–1461.
16 J. F. C. Kingman, *Poisson Processes*, Oxford University Press, New York, 1993.
17 S. M. Ross, *Simulation*, Academic Press, 2006.
18 D. Wood, M. Requa and A. Cleland, *Rev. Sci. Instrum.*, 2007, **78**, 104301.
19 S. Zheng, M. Liu and Y.-C. Tai, *Biomed. Microdevices*, 2008, **10**(2), 221–231.
20 www.iso.org.
21 T. W. Britton, L. U. Jiuliu and J. L. Rose, *US. Pat.*, 8154273, 2012.
22 N. N. Watkins, U. Hassan, G. Damhorst, H. Ni, A. Vaid, W. Rodriguez and R. Bashir, *Sci. Transl. Med.*, 2013, **5**, 214ra170.
23 N. N. Watkins, S. Sridhar, X. Cheng, G. D. Chen, M. Toner, W. Rodriguez and R. Bashir, *Lab Chip*, 2011, **11**, 1437.
24 U. Hassan, N. N. Watkins, C. Edwards and R. Bashir, *Lab Chip*, 2014, **14**, 1469–1476.